Nano Energy 115 (2023) 108735

Contents lists available at ScienceDirect

Nano Energy

journal homepage: www.elsevier.com/locate/nanoen

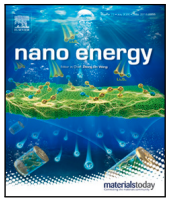

Full paper

Optimisation-driven design of sliding mode triboelectric energy harvesters

Lucas Q. Machado [a,*], Huai Zhao [b], Morteza Amjadi [c], Huajiang Ouyang [b], Philippe Basset [d], Daniil Yurchenko [e]

[a] IMPEE, Heriot-Watt University, Edinburgh, UK
[b] University of Liverpool, Liverpool, UK
[c] James Watt School of Engineering, University of Glasgow, Glasgow, UK
[d] Univ Gustave Eiffel, CNRS, ESYCOM, F-77454, Marne-la-Vallée, France
[e] ISVR, University of Southampton, Southampton, UK

ARTICLE INFO

Keywords:
Global optimisation
Triboelectricity
Energy harvesting

ABSTRACT

With the increasing demand of emerging technologies for autonomous sensing, the modelling and optimisation of complete energy harvesting systems are essential to achieve efficient power output. To date, most of the optimisation efforts in enhancing the performance of triboelectric energy harvesters have been focused on the improvement of material properties and on the establishment of figures of merit to assist in the definition of parameters. However, these efforts do not consider the complex relationship between the device structure and power output, physical constraints in place, and varying excitation conditions. This paper fills that gap for the first time by applying an optimisation algorithm to establish mechanisms for optimisation-driven design of sliding-mode triboelectric energy harvesters. A global optimisation methodology is developed to improve its performance, having experimentally validated the numerical model adopted. This work highlights the need for a more robust design framework for applications of triboelectric energy harvesting and proposes a hybrid approach combining the finite element method with analytical models to consider different energy harvesting parameters including the degradation of the charge transfer efficiency due to the edge effect. A novel high-power output sliding-mode triboelectric energy harvesting concept is proposed and its performance is optimised, using the proposed methodology.

1. Introduction

The increasing interest in smart devices has driven the development of sensor systems that connect and exchange data over the internet and communication networks. According to a report released in 2021 by the Grand View Research (GRV), the global retail market of the Internet of Things is expected to reach USD 182.04 billion by 2028, expanding at a compound rate of 26.0% from 2021, when it was valued at USD 31.99 billion [1]. This trend spurs the growing need for optimised solutions in the fields where real-time information facilitates enhanced responses and decisions. Some of these application domains are security and surveillance, energy consumption, agriculture automation, healthcare and medicine, smart cities and houses, and traffic management [2]. Most of these applications, however, face a significant challenge due to their dependency on batteries as power sources, which often suffer from limited life cycles [3].

The success of many smart applications relies on reducing the costs associated with regular replacement of depleted batteries. Battery-free self-powered sensors enable maintenance-free applications and resolve the problem related to the enormous amount of toxic waste disposal of batteries [3,4]. Therefore, energy harvesting is a promising technology to be integrated into smart systems, enabling self-powered sensing in urban environments. Energy can be harvested in urban environments from structural vibrations, in-pipe water flow, airflow, running vehicles and trains, etc. The goal is to convert kinetic energy present in such systems into electricity through transduction mechanisms, including piezoelectric, electromagnetic, electrostatic/triboelectric solutions. The ultimate goal of energy harvesting technologies is to balance the energy harvested from the environment and the energy required for the continuous operation of a targeted application.

The triboelectric transduction mechanism presents many attractive advantages for energy harvesting applications. It possesses high efficiency, with reported 85% mechanical energy conversion [5], it is easy [6] and inexpensive [7] to manufacture, it yields high power output [8], is environmentally friendly [9], and can be employed in several applications [10–12]. Consequently, it has been observed significant progress in the development of triboelectric harvesters for

* Corresponding author.
E-mail address: lq14@hw.ac.uk (L.Q. Machado).

https://doi.org/10.1016/j.nanoen.2023.108735
Received 22 February 2023; Received in revised form 18 July 2023; Accepted 20 July 2023
Available online 22 July 2023

wearables [13,14], blue energy [15–17], and self powered-sensors [18–22]. Triboelectric energy harvesters are presented in several operating modes, e.g., vertical contact separation, lateral contact-sliding, single-electrode, and freestanding. This work will explore and address the challenges in the design of sliding mode triboelectric energy harvesters assisted by the optimisation methodology proposed by [23–25] initially applied for piezoelectric energy harvesting systems.

The key to enable self-powered autonomous sensing lies on the development of application-oriented harvesting devices. In the triboelectric energy harvesting field, a great number of harvesters has been reported in the literature offering some solutions, e.g., reliable modelling [26,27], enhanced material properties [28–31], and circuit topology [32,33]. Typically the optimisation has been focused on a single component of a concept, instead of considering the optimisation of a device as a whole. For instance, most optimisation efforts are placed in the material science aspect as the usual means of optimising triboelectric energy systems, e.g., by increasing the surface charge density of the triboelectric layer, by increasing the capacitance variation of the transducer through micro-surface-patterning to increase the contact area [34–36], by altering the composition of friction materials [37], and through the improvement of dielectric properties [38,39].

All these efforts are necessary for the development of energy harvesting technologies, which have emerged as a feasible power supply alternative for embedded systems. However, it is also essential to employ resources that can help to design an embedded system, which is capable of, first, getting through the initial power-on reset, and, second, outliving the lifespan of the self-sustaining embedded system. These are the two basic essential requirements for achieving perpetual operation, which is the fundamental objective of any harvester.

In [23], and [25] the authors developed and implemented an optimisation methodology that considered the entire harvesting system and the multiple parameters associated with the harvester's operation under several operating conditions [24]. The framework presented in their work was applied to piezoelectric harvesters only, however, this methodology can be extended to other energy harvesting techniques. Therefore, an adapted framework is proposed to take into account the features and particularities of the forced triboelectric energy harvesting technique. Thus, this paper establishes mechanisms for optimisation-driven design of sliding-mode triboelectric harvesters by means of a global optimisation procedure. The objective function is defined based on leading design parameters such as length, thickness, width, number and width of hollowed-out units forming the grating pattern in sliding-mode triboelectric harvesters, the distance between the hollowed-out units, number of triboelectric layers, and optimal resistance. Section 2 presents the electromechanical model and a more flexible V-Q-x relationship for sliding-mode triboelectric generators. Section 3 presents the FEM model and the analysis of the charge transfer efficiency degradation due to the edge effect. Section 4 presents the experimental analyses conducted to validate the model adopted. Section 5 presents the optimisation approach adopted and explains its features and algorithm. Section 6 presents results obtained through the optimisation algorithm and shows the level of improvement provided when compared to non-optimised conditions. Here, a new sliding-mode triboelectric harvester design is proposed, driven by the optimisation procedure. A summary of the findings is presented as follows:

- Although the model of the sliding-mode triboelectric device has been proposed before, this paper highlights the need for the implementation of a device-oriented optimisation methodology. There is no account for such an implementation being applied to triboelectric harvesters thus far. Previous works select model parameters rather randomly, either from limited numerical simulation analysis or from the experience of previous experiments. In the present paper, the authors go much further, not only clearly showing how the parameters of the model should be selected, but also demonstrating the importance of optimisation, which substantially increases the TENG performance (see Fig. 12).
- To date, no sliding-mode triboelectric harvester designs have adopted a nonidentical grated pattern between the width of the hollowed-out units and the distance between them. This paper explores this aspect for the first time and indicates that the width of the hollowed-out units must be greater than the distance between them.
- The results show that the optimal number of grating units tends to decrease as the frequency increases, which shows its dependency on the excitation conditions and not only on the topology of the layers.
- This paper incorporates the result of FEM analyses into the analytical equations to account for the edge effect, which is also done for the first time in the literature. This is achieved through the use of a charge-transfer efficiency parameter, which is a function of the unit aspect ratio of the dielectric film. With this, the model overcomes the edge effect limitation by accounting for the charge transfer degradation, present in designs characterised by a lower unit aspect ratio. Therefore, this work can more precisely establish the optimal performance region as it considers the trade-off between the gain from more charge cycles and the loss from charge transfer degradation at low unit aspect ratio designs.
- The influence of the ratio between the length of the oscillating layers and the length of the stationary layers was analysed for the first time. It has been shown that the optimal length ratio is not 0.5 as mostly adopted in the literature, but that it varies, depending on the other parameters, such as the excitation frequency and resistance.
- The completely new device concept is proposed, based on the sliding mode triboelectric effect. The uniqueness of the proposed concept is its ability to be pre-tuned to any excitation frequency, since the natural frequency of the entire device is independent of the proposed global optimisation approach, making the device suitable for a great variety of applications.

2. Electric model of the device

Fig. 1-I schematically illustrates the structure and operation mechanism of our proposed energy harvester. The triboelectric energy harvesting is triggered by the friction between positively and negatively charged materials. In the proposed device, they are represented by an oscillating electrode on the top and a stationary electrode on the bottom (both positively charged) and a stationary dielectric film (negatively charged) attached to the bottom electrode forming *a variable capacitance*. This configures the conductor-to-dielectric mode, where one of the electrodes is not attached to a dielectric material [9]. As the top electrode oscillates along the stationary component, the capacitance varies and, during the first oscillations, the dielectric film generates charges due to triboelectric effect. Consequently, electrons are transferred between the electrodes during the following mechanical oscillations based on in-plane electrostatic induction [40]. Fig. 1 depicts this process in four phases after the initial charging of the triboelectric layer. First, (Fig. 1-II), the two electrodes and the dielectric film are fully overlapping and we assume that the negative charge embedded in the triboelectric layer will remain constant during the electromechanical energy conversion process. We also assume that those triboelectric charges are uniformly distributed in the dielectric on top of its surface. This results in a net positive charge in the top electrode. As the top electrode slides (Fig. 1-III), the unbalanced negative charges on the dielectric film induces an electrical potential which drives electrons from the bottom electrode to the top electrode. The electric potential reaches its maximum value when the top electrode is at its fully displaced position (Fig. 1-IV, where the negative triboelectric charges are compensated by the induced charges. As the top electrode slides back, the electrons are driven back to the bottom electrode (Fig. 1-V). Under continuous oscillation, an alternating current is generated.

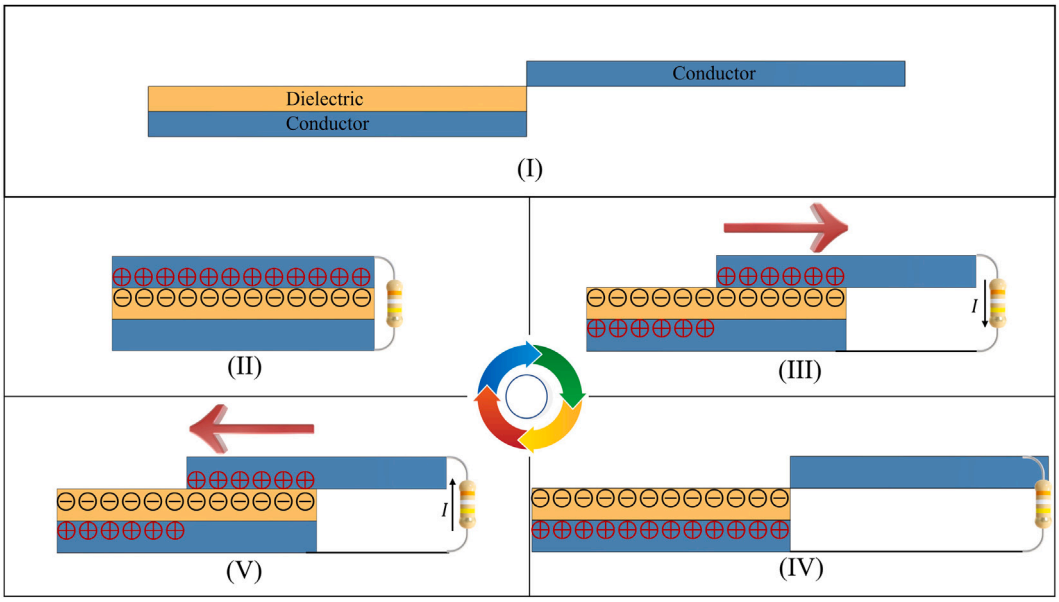

Fig. 1. Triboelectric energy harvesting mechanism under slide mode.

There are two basic categories of models used to model triboelectric systems [41]. The first was developed based on the formal electromagnetic theory [41–43] as described by Maxwell's laws and the resultant general theory of the electric field and displacement current. The second model was developed based on the lumped parameter circuit theory [40,44], which is adopted in this paper. For the purpose of this study, the sliding-mode triboelectric harvester is modelled as a voltage source corresponding to the open-circuit voltage of the triboelectric harvester in series with the variable capacitor [41,42,45]. If the equivalent electric model is connected in series to a load R, the governing Equation of the triboelectric generator is expressed as [40,46]:

$$V = R\frac{dQ}{dt} = -\frac{Q(x)}{C(x)} + V_{OC}(x) \tag{1}$$

where V is the voltage across the resistive load R, Q is the transferred charge between electrodes during the motion of the top electrode, $C(x)$ is the capacitance between the two electrodes, and $V_{OC}(x)$ is the open circuit voltage. The capacitance and the open circuit voltages are functions of the displacement x of the oscillating electrode, as follows:

$$C(x) = \frac{\varepsilon_0 \varepsilon_r A_1(x)}{t_d} \tag{2}$$

$$V_{OC}(x) = \frac{\sigma A_2(x) t_d}{\varepsilon_0 \varepsilon_r A_1(x)} \tag{3}$$

where A_1 is the overlapping area between the oscillating and fixed electrodes and A_2 is the area of the dielectric film not overlapped by the sliding electrode, t_d is the thickness of the dielectric film, σ is the surface charge density, ε_0 is the dielectric permittivity of vacuum, and ε_r is the relative dielectric permittivity of the dielectric film.

Fig. 2 presents the film pattern described by the analytical model. The width of the hollowed-out units is given by d, while the distance between hollowed-out units is given by δ, as follows:

$$d = \frac{L}{N + N r_{\delta|d} + r_{\delta|d}}, \tag{4}$$

$$\delta = r_{\delta|d} d \tag{5}$$

where L is the length of the longer film, $r_{\delta|d}$ is a dimensionless parameter used to establish the relationship between δ and d, and N is the number of hollowed-out units on the longer film (Fig. 2(a)). This approach is adopted to allow optimising the ratio between the width of the hollowed-out units (d) and the distance between them (δ). Given the hollowed-out units, the overlapping area between the upper electrode and the dielectric film varies due to their relative displacement. Therefore, A_1 and A_2 are functions of the mobile electrode displacement x:

$$A_1 = A_0 + \begin{cases} \text{if } \delta \geq d \\ \begin{cases} w_0\left(\delta - x_0\right)(n+1), & x_0 \in [0, d] \\ w_0\left(\delta - d\right)(n+1), & x_0 \in (d, \delta] \\ w_0\left(x_0 - d\right)(n+1), & x_0 \in (\delta, d+\delta], \end{cases} \\ \text{if } \delta < d \\ \begin{cases} w_0\left(\delta - x_0\right)(n+1), & x_0 \in [0, \delta] \\ 0, & x_0 \in (\delta, d] \\ w_0\left(x_0 - d\right)(n+1), & x_0 \in (d, d+\delta], \end{cases} \end{cases} \tag{6}$$

and,

$$A_0 = l\left(w - w_0\right) \tag{7}$$

$$A_2 = w_0\delta(N+1) + l(w - w_0) - A_1, \tag{8}$$

where w and l are the width and the length of the film, w_0 is the height of the hollowed-out unit, and N is the number of hollowed-out units on the longer film. The length, L, presented in (4) must satisfy the following equation:

$$L = (\delta + d)N + \delta. \tag{9}$$

Note that $N = 0$ results in $\delta = L$. A function $x_0(x)$ is introduced in the calculation of the overlapping area and it informs the relative displacement between hollowed-out units on the film and on the electrode, which is reset every time they completely overlap each other:

$$x_0 = rem(|x|, \delta + d), \tag{10}$$

where $rem(\cdot)$ is the remainder operator. The length of the carriage (l) is determined depending on the number of hollowed-out units (n) it has, which is a fraction ($r_{l|L}$) of the number of hollowed-out units (N) on the extended film rounded to the nearest integer, as presented in the following equation:

$$n = N - \lfloor r_{l|L} N \rceil, \tag{11}$$

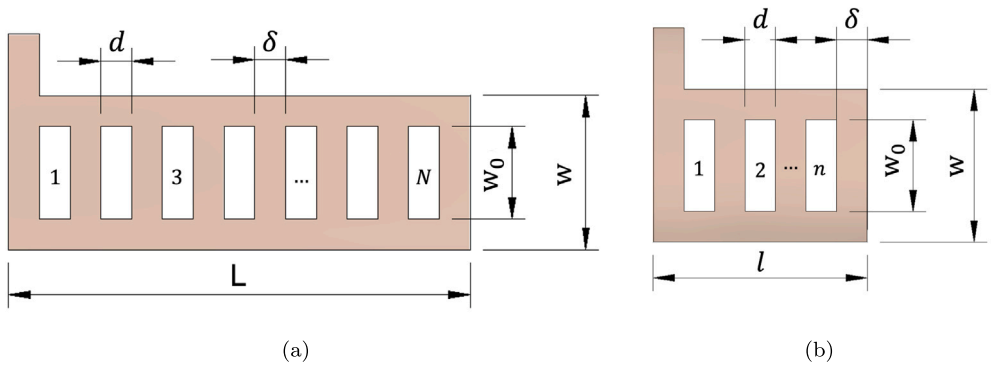

Fig. 2. Grating pattern: (a) film and (b) sliding electrodes can assume distinct lengths, having different number of hollowed-out-units.

thus, the length of carriage is determined by:

$$l = L - (N - n)(\delta + d), \tag{12}$$

which can be understood as the resultant length after the removal of $(N - n)$ grating units $(\delta + d)$ from the larger film.

In general, a number of layers allowed along the thickness of a device depends on the thickness of the dielectric film and electrode layers. One triboelectric unit is composed of one electrode-dielectric-electrode set, i.e., three layers (see Fig. 1), where the top electrode moves with respect to the dielectric film and the electrode attached to it. The thickness of the dielectric (t_d) can be optimised while the thickness of the electrodes (t_e) remains constant. Therefore, the number of layers (n_{dl}) can be defined based on the resultant thickness of the dielectric layer:

$$n_{dl} = \left\lfloor \frac{T - t_e}{(t_d + t_e)} \right\rfloor. \tag{13}$$

where T is the device thickness.

3. Edge effect analysis via FEM

The edge effect is characterised by the uneven distribution of charges at the edges of the electrodes of the triboelectric unit [47], observed in a concentration of charges at the edges of the dielectric [48]. Consequently, under such circumstances, the electric field distribution inside the dielectric is also non-uniform, contrary to the capacitive model adopted, which considers a uniform electric field distribution. Two conditions are necessary to neglect the edge effect: first, the length of the dielectric film must be much larger than its thickness, and, second, the separation distance must be less than 0.9 L [47]. This will ensure that the uniformity of the electric field is predominant, although the edge effect is always present at the boundaries of a real system. A FEM model was built in COMSOL to study the influence of the electric field and the edge effect over the charge transfer efficiency (η_{CT}). The model consists of a dielectric layer placed between two electrodes, configuring the conductor-to-dielectric type. The bottom electrode and the dielectric layer are fixed while the top electrode slides, inducing triboelectrification. Each layer is 50 mm long and 25 mm wide. The two electrodes are 0.01 mm thick while the thickness of the dielectric layer is 0.5 mm. The surface charge density σ adopted for all simulations is 80 $\mu C/m^2$, a value calculated based on the experimental results. The output voltage of the sliding-mode triboelectric energy harvester is measured first, and then the value of the charge density is adjusted in numerical simulation to fit the theoretical voltage with the measured voltage. A similar value was also reported in [49]. Note that the model is built for the case when $N = 0$, which leads to $\delta = L$. This approach is considered because the edge effect is observed due to the increase of the δ/t_d ratio, as reported by [50]. Fig. 3(a) illustrates the arrangement of the model simulated in COMSOL while Fig. 3(b) presents the FEM results for the potential distribution when $x = L/2$. Fig. 3(c) presents the surface charge at x varying from 5 mm to 45 mm. Figs. 3(d) and 3(e) present the charge transfer under short-circuit condition and the open circuit voltage, respectively. There are three responses for the slide-mode triboelectric generator in Figs. 3(d) and 3(e). The first was obtained analytically (red), the second is the result from the analytical model adapted by η_{CT} (magenta), and the third is the response obtained from FEM simulation (blue). Fig. 3(f) shows the charge transfer efficiency surface as a function of the overlap and unit aspect ratios.

The FEM simulations are performed in open-circuit as well as in short circuit conditions. In the open-circuit configuration, the floating potential is initially defined as zero (discharged capacitor) on the upper surface of the top electrode and on the lower surface of the bottom electrode, i.e., their total surface charge density is also zero. In the short-circuit configuration, the same surfaces are connected to a common ground. Three main sets of results are extracted from these simulations: the $V_{OC}-x$, the $Q_{SC}-x$, and the $\eta_{CT}-\delta/t_d$ responses, where η_{CT} is defined as the charge transfer efficiency, and the δ/t_d as the unit length over dielectric thickness aspect ratio. The first two relationships ($V_{OC} - x$ and $Q_{SC} - x$) are presented for validation purposes while the third ($\eta - \delta/t_d$) will assist in understanding some consequences of the edge effect in the charge transfer and its influence in improving the analytical $V_{OC} - x$ and $Q_{SC} - x$ relationships.

In the open-circuit configuration, the open-circuit electric potential difference between the top and bottom electrodes (V_{OC}) in the FEM model is probed as the top electrode slides on the dielectric layer. As expected, V_{OC} increases as the overlap distance $(L-x)$ decreases. Also, as x approaches L, the curve $V_{OC} - x$ approaches asymptotically to infinity because the overlap area tends to zero $(A_1(x) \to 0)$, as presented in Eq. (3). Fig. 3(e) shows that there is a good agreement between FEM (blue) and analytical (red) results up to the point where $(L - x) \gg t_d$ is valid. As the overlap area decreases, so increases the discrepancy between analytical and FEM results. This effect has been discussed by [48], where the authors point out that the electric field distribution in the x-axis becomes more prominent at the edges and can no longer be neglected if the overlap distance is small enough to be compared to the thickness of the dielectric layer $((L - x) \sim t_d)$. For this reason, a modified, semi-analytical model is proposed.

In the short-circuit configuration, the amount of transferred charges Q_{SC} in the FEM model is probed at the bottom electrode as the top electrode slides on the dielectric layer. Fig. 3(d) presents the $Q_{SC} - x$ responses of the analytical model (red), analytical model modified by η_{CT} (magenta), and the FEM model (blue). In all three cases, the $Q_{SC}-x$ relationship is linear, as predicted by Eq. (14):

$$Q^{SC}(x, \delta/t_d) = xw\sigma, \tag{14}$$

where x represents the relative displacement between the top electrode and the dielectric layer attached to the bottom electrode. Therefore, the

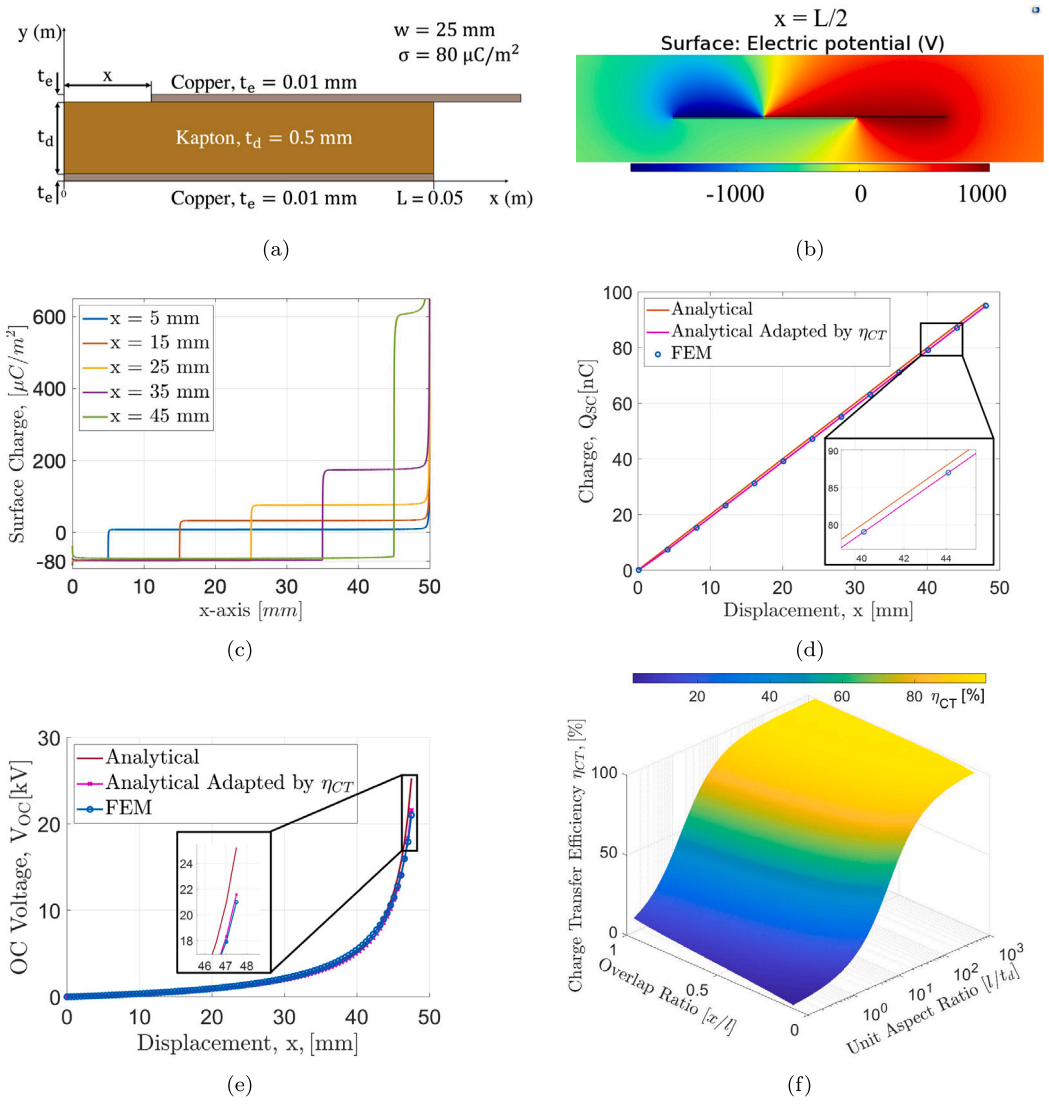

Fig. 3. FEM simulations results in comparison with response obtained via analytical formulation: (a) FEM model built in COMSOL, (b) surface electric potential for $x = L/2$ mm in open-circuit condition from FEM simulation in COMSOL, (c) surface charge distribution on top electrode in open-circuit voltage condition, (d) charge transfer under short-circuit condition, (e) open-circuit voltage, and (f) charge transfer efficiency dependency to the unit aspect ratio from FEM simulations.

total charge transferred at full displacement is given by Eq. (15):

$$Q^{SC}(x = L, \delta/t_d) = Lw\sigma, \tag{15}$$

Fig. 3(d) indicates that there is a good level of agreement between the analytical and FEM results with around 1% error as $x \to L$. In this case, approximately the same absolute charge transferred discrepancy is observed along the entire displacement distance.

There is a theoretical limitation when the unit aspect ratio $(L - x)/t_d$ is small: if the theoretical linear equations are used to model triboelectric systems, where the thickness of the dielectric is of the same order of magnitude or greater than $(L - x)$, the outcomes will exceed the potentially achievable practical values, as presented in Fig. 3(e) for V_{OC}. [9] showed through FEM simulations that the mismatch given by the analytical model is caused by its inability to account for the edge effect, which degrades the charge transfer efficiency (η_{CT}) as the unit aspect ratio (δ/t_d) decreases. In this sense, this work proposes a novel contribution, where the analytical model is adapted to consider the charge transfer efficiency, as defined by Eqs. (16) and (17):

$$\eta_{CT}(x, \delta/t_d) = \frac{Q_{SC}^{FEM-CT}(x, \delta/t_d)}{Q_{SC}^{Total}(x, \delta/t_d)}, \tag{16}$$

$$\sigma_{eq} = \eta_{TC}\sigma, \tag{17}$$

where Q_{SC}^{FEM-CT} is the amount of transferred charges (TC) obtained via FEM simulation, considering the edge effect, Q_{SC}^{Total} is the total amount of charges when the edge effect is neglected, and σ_{eq} is the equivalent charge density accounting for the edge effect by considering the charge transfer degradation due to the decrease of the unit aspect ratio.

Therefore, the model incorporating η_{CT} becomes semi-analytical as it relies on the charge transfer efficiency curve provided through FEM simulation, as shown in Fig. 3(f). The influence of the semi-analytical model is observed in Figs. 3(d) and 3(e), which is able to improve the prediction of the open-circuit voltage near the edges and the amount of charge transferred. The error in predicting the open-circuit voltage near the edges decreased from 20% to 2% while the error in predicting the short-circuit charge transferred decreased from 3.3% to 2.0%.

4. Model validation via experimental testing

The model developed in Section 2 is implemented and simulated via MATLAB/Simulink to allow predicting the behaviour of the sliding-mode triboelectric harvester and for subsequent optimisation. The validation of the model is performed through the prototype presented in

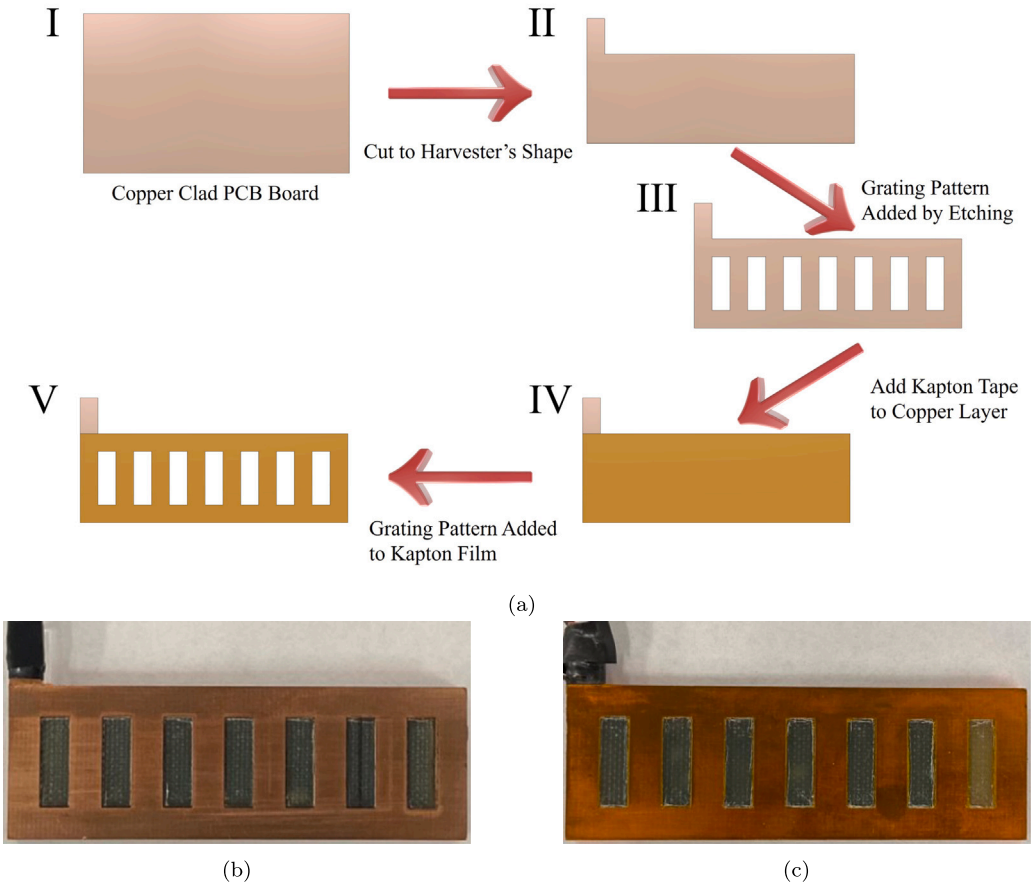

Fig. 4. (a) Prototype Preparation: Sliding-mode triboelectric harvester: I — Copper Plate; II — Copper clad pcb board cut to final shape; III — Grating pattern added by etching copper clad board; IV — Kapton layer added; V — Grating pattern added to Kapton film. (b) Electrode and (c) Electrode with Kapton film added.

Fig. 4. Fig. 4(a) presents the manufacturing process of the prototype: Initially, (I) a copper clad PCB board is (II) cut to the harvester's shape, and then (III) etched to add the grating pattern. Next, (IV) a Kapton tape is added to the grated copper board and (V) manually grated. Fig. 4(b) presents the electrode, i.e., the grated copper board without the Kapton tape, while Fig. 4(c) presents the grated copper board with the grated Kapton tape attached to it. Thus, sliding-mode triboelectric energy prototype is composed of two geometrically identical parts with seven hollowed-out units each, as presented in the CAD model of the prototype in Fig. 5-III. The unit aspect ratio of the prototype is $\delta/t_d = 100$, therefore the edge effect is negligible. Figs. 5-II and IV depict the electrode on the top and the dielectric film attached to the other electrode on the bottom. Fig. 5-V shows the experimental rig built to test the performance of the device and validate the analytical model presented in Section 2.

The dielectric film used in the experimental analyses is the 25 μm thick Polyimide film (KPT-2485), known as Kapton, while the electrodes are manufactured from 1 mm thick copper clad boards. Two layers of Kapton tape are added to the bottom electrode, creating a 50 μm thick film. The sliding-mode triboelectric harvester is connected to 10 MΩ and 280 kΩ resistors in series. The 10 MΩ resistor drops the voltage to a secure level to be recorded by the NI DAQ 6008 which is connected across the 280 kΩ resistor. The vibration table is driven by a motor through a crank and a sliding mechanism, which provides a harmonic excitation with 20 mm amplitude displacement, equivalent to $2(\delta + \mathrm{d})$ units. The ADXL 203eb accelerometer was attached to the table (see Fig. 5-V) to monitor the input acceleration. The acceleration and the harvester voltage data were read through the data acquisition module NI-6008 and processed in LabView 2020.

Fig. 6 compares the experimental data with the output of an equivalent triboelectric model under in-plane sliding mode. The experimental data are presented as recorded through the data acquisition card, without any filtering or processing. One can observe satisfactory agreement between the numerical and experimental results for a charge density of 80 $\mu C/m^2$. The model and its prototype successfully respond to the variations in the overlapping area due to the hollowed-out units' displacement as the top electrode is forced to oscillate.

Furthermore, the prototype is analysed under 6 operating frequencies ranging from 0.89 to 4.25 Hz. The load resistance of 280 kΩ remains the same throughout the analyses as well as the displacement amplitude of 20 mm for each selected frequency. The root mean square (RMS) of the experimental voltage output at each excitation frequency is calculated as follows:

$$V_{RMS} = \sqrt{\frac{1}{N}\sum_{n=1}^{N} |V_n|^2}, \tag{18}$$

where N is the number of samples. The resultant root mean square power is calculated according to Eq. (19):

$$P_{RMS} = \frac{V_{RMS}^2}{R}. \tag{19}$$

The experimental RMS voltage and power are then compared against that of the numerical response, as presented in Fig. 7(a). The numerical and experimental values show good agreement, as indicated by a mean error under 4%.

5. Optimisation algorithm

The surrogate optimisation algorithm from the MATLAB optimisation toolbox is selected due to the following features: it is designed to

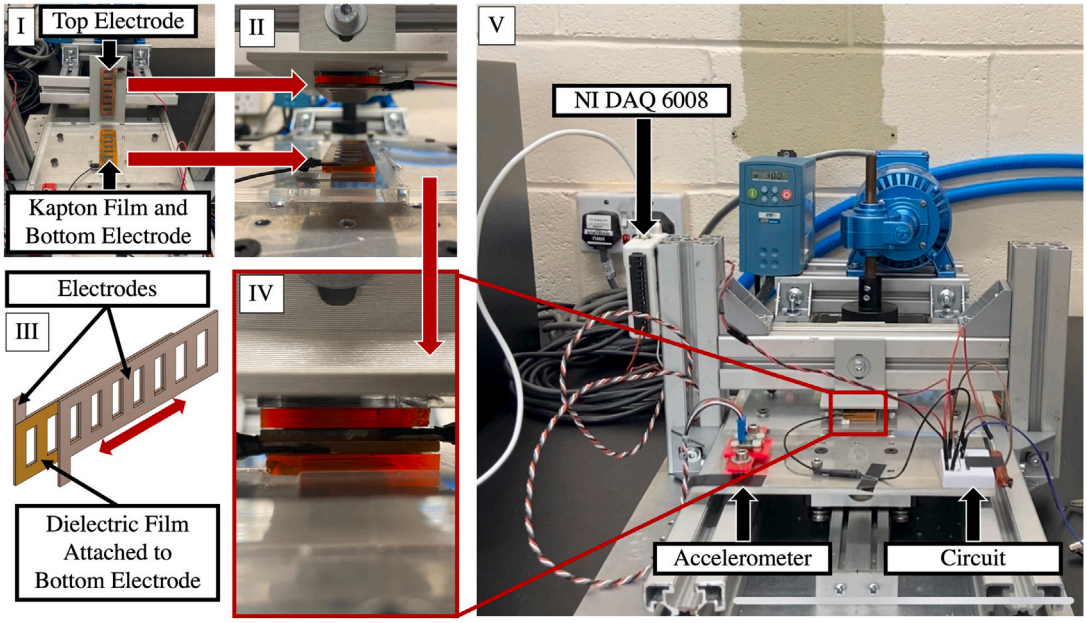

Fig. 5. Sliding-mode triboelectric harvester and experimental rig: I — Top electrode and Kapton film attached to bottom electrode detached; II — Top and bottom units before contact; III — CAD model of the harvester indicating the slide-mode operation; IV — Harvester arrangement under operation in slide-mode; V — Experimental rig.

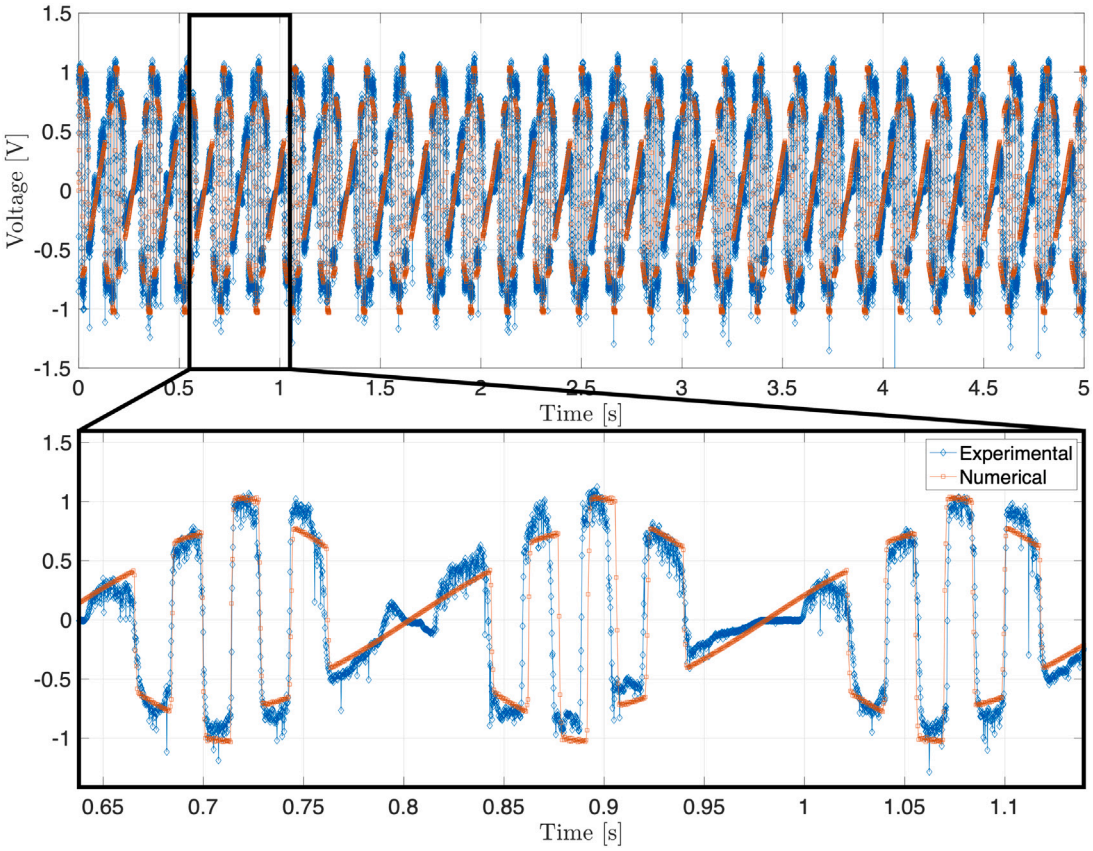

Fig. 6. Numerical and experimental comparison for a sliding-mode triboelectric harvester.

optimise expensive objective functions, it is by constitution a global solver, and it does not require an initial guess, only upper and lower boundaries. The basic concept of the surrogate algorithm is that it creates a surrogate objective function, i.e., a model that emulates the original function through interpolation techniques. In this work the objective function is defined by Eq. (20), which aims to maximise the power output of the harvester. This model is then used to find better points to be evaluated, where each point refers to a design and its performance. Therefore, the optimisation algorithm evaluates the objective function based on the average power output performance

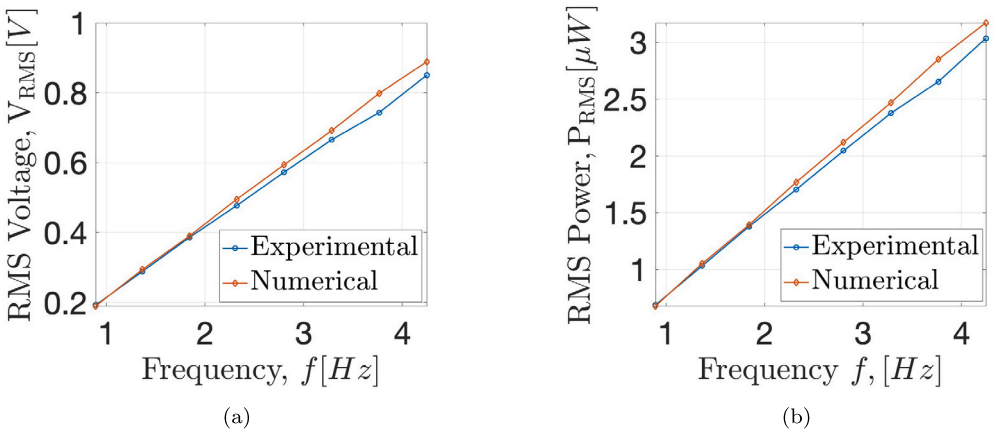

Fig. 7. Prototype performance considering one triboelectric unit (conductor-electrode-conductor): Experimental and numerical response of the triboelectric unit under varying excitation frequency for the (a) RMS voltage and (b) RMS power.

achieved by the device under the parameter values that were selected.

$$\max_{\mathbf{p}_i} P_{AVG}(\mathbf{p_i}),\ b_{li} \le \mathbf{p}_i \le b_{ui},$$
$$P_{AVG}(\mathbf{p}_i) = \frac{1}{t}\sum_{j=1}^{n_{dl}} E_j(\mathbf{p}_i), \tag{20}$$

where $E_j(\mathbf{p}_i)$ is the energy delivered by each layer, t is the total time over which the energy is generated, b_{li} and b_{ui} are the lower and upper bounds of the ith parameter $\mathbf{p}_i$.

The algorithm alternates between the tasks of creating the surrogate and searching for the minimum. The surrogate is created by evaluating the objective function at quasi-random points within the predefined upper and lower bounds of each parameter. Next, a smooth function is created by interpolating and extrapolating those points, which characterises the surrogate. This process is repeated at each iteration, i.e., more points are generated to evaluate the objective function and then added to the surrogate. The algorithm interpolates and extrapolates all evaluated points, updating the surrogate. The next task is to search for the minimum, where other two sub-tasks are carried out: the search for a better objective function value around an existing point by refining it, and exploring non-assessed regions. This second step improves the chances of finding a global minimum by not focusing around one potential point only. The surrogate algorithm alternates between the construction of the surrogate and the search for a minimum until reaching the stop condition, which can be set by time or iteration limit. Here the iteration criteria is adopted and limited to 300 global iterations. Each global iteration has a local iteration for each optimisation parameter, e.g., if the objective function depends on five parameters, a total of 1500 parameter combinations are assessed in each optimisation procedure.

6. Results

The optimisation procedure is conducted considering up to five optimisation parameters: the ratio between the length of the oscillating electrode and the length of the stationary triboelectric film and electrode ($r_{l|L}$), the thickness of the dielectric layers (t_d), the ratio ($r_{\delta|d}$) between the width of the hollowed-out units (d) and the distance (δ) between them, the electrical resistance (R), and the number of hollowed-out units on the dielectric film (N), thus $\mathbf{p} = [R, t_d, r_{\delta|d}, r_{l|L}, N]$. All device parameters are determined as a result of optimising $\mathbf{p}$, e.g., the length of the carriage (l) is determined by the number of hollowed-out units (n) it has according to Eq. (12). The parameter n is a direct result of the ratio $r_{l|L}$, optimised in the process via Eq. (11). The width of the hollowed-out unit and the distance between them are determined through the optimised ratio parameter $r_{\delta|d}$, as presented in Eq. (4). The optimised number of triboelectric layers within the thickness of the harvester is directly determined by the optimal thickness of the dielectric film (t_d), as the thickness of the electrodes remains constant (Eq. (13)). The optimisation of the resistance is included because there is no analytical solution to predict it beforehand in slide-mode triboelectric energy harvesting systems. Note that, apart from the number of hollowed-out units and length, all the other parameters within an optimised device are always the same in all layers and electrodes.

The optimisation procedure is applied to the built prototype in Section 6.1. The prototype is optimised under two conditions. In the first condition, the prototype is optimised considering only the ratio ($r_{\delta|d}$) and the resistance (R). In the second condition, the optimisation of the prototype is extended to consider four parameters: t_d, $r_{\delta|d}$, N, and R. Section 6.2 introduces the new slide-mode triboelectric energy harvester design, while Section 6.3 addresses its electro-mechanical optimisation considering five parameters: $r_{l|L}$, t_d, $r_{\delta|d}$, N, and R. The results presented in the following subsections for each device size and excitation frequency are the best values out of three optimisation rounds, i.e., the optimisation is repeated three times allowing different points to be analysed to assure that the optimal set of parameters has been determined.

6.1. Prototype optimisation

Table 1 presents a summary of the optimised triboelectric parameters considering that the objective function directly depends only on the resistance (R), i.e., $\mathbf{p} = [R]$. The optimisation procedures were carried out under harmonic excitations of the same level experienced experimentally by the prototype, i.e., at a constant sinusoidal displacement of 20 mm amplitude and at oscillating frequencies ranging from 0.89 to 4.25 Hz (see Fig. 7(a)). Apart from the optimised resistance, all other dimensions and properties were kept the same as in the prototype, including the thickness of the dielectric film, the number of dielectric layers in the device, the thickness of the electrode, the width of the hollowed-out units, and the number of hollowed-out units.

Fig. 8 graphically presents the results shown in Table 1. It should be observed that the average power output per displacement cycle is kept at 0.12 mW/Hz, indicating that the average power tends to increase linearly within the frequency range analysed, as presented in Fig. 8(a). Fig. 8(b) presents the shape of the curve for rms voltage and optimal resistance for the given excitation frequencies, indicating that the optimal resistance and rms voltage decrease at higher frequencies. Compared with the conditions at which the prototype is experimentally assessed, it can be concluded that selecting the optimal load resistor boosts the power output up to around 20 times, from a micro-power level in Fig. 7(b) to a mili-power level in Fig. 8(a). Note that the values

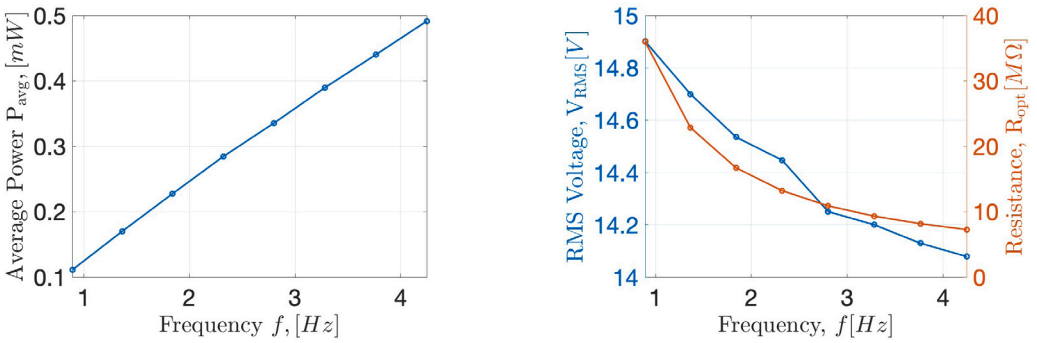

Fig. 8. Prototype Optimisation for R and $r_{\delta|d}$: (a) RMS power output, (b) RMS voltage, and optimal resistance for increasing excitation frequencies.

Table 1
Optimisation of the Resistance R applied to the prototype configuration obtained via surrogate optimisation under harmonic excitation.

Device configuration L = 75 mm, W = 25 mm, $W_0 = W - \delta$, $\delta = d = 5$ mm t_d = 50 μm l = L, N = n = 7, n_{dl} = 18, σ = 80 μC/m^2			
	Optimisation parameters	Optimised parameters	
f_{exc} Hz	R MΩ	P/f mW/Hz	V_{RMS} V
0.89	36	0.12	14.90
1.36	23	0.12	14.70
1.84	17	0.12	14.54
2.32	13	0.12	14.45
2.80	11	0.12	14.25
3.28	9	0.12	14.20
3.76	8	0.12	14.13
4.25	7	0.12	14.08

Table 2
Optimisation of the ratio $r_{\delta|d}$ and Resistance R applied to the prototype configuration obtained via surrogate optimisation under harmonic excitation.

Device configuration L_d = 50 mm, W_d = 25 mm, $W_0 = W_d$ - 2δ, t_d = 50 μm $l_c = L_d$, N = n = 7, n_{dl} = 18, σ = 80 μC/m^2						
	Optimisation parameters		Optimised parameters			
f_{exc} Hz	$r_{\delta|d}$ –	R MΩ	δ mm	d mm	P_{avg}/f mW/Hz	V_{RMS} V
0.89	0.62	47	3.89	6.27	0.15	18.97
1.36	0.63	30	3.92	6.23	0.15	18.57
1.84	0.64	21	3.96	6.19	0.15	18.23
2.32	0.64	17	3.96	6.19	0.15	18.09
2.80	0.63	14	3.92	6.23	0.15	17.93
3.28	0.65	12	4.00	6.15	0.15	17.73
3.76	0.63	10	3.92	6.23	0.14	17.75
4.25	0.64	9	3.96	6.19	0.14	17.63

in Fig. 7(b) are for a single triboelectric unit, thus, for a fair comparison, they are multiplied by 18, which is the number of triboelectric units fitted within the harvesting device.

Next, the ratio $r_{\delta|d}$ is added to be assessed by the objective function to study the effect of allowing δ and d to assume distinct values. Table 2 presents the optimisation results obtained. Note that the optimal ratio between δ and d is found around 0.63, indicating that the performance of the harvester is improved when the distance δ between the hollowed-out units is slightly lower than their width d. The results also show that, at lower frequencies, the power output per cycle was improved by 25.0%, while around 16.7% at higher frequencies. The voltage and optimal resistance kept the same pattern as presented in Table 1, decreasing as the frequency increased.

Further analysis is conducted to observe how the average power output varies with respect to R and $r_{\delta|d}$ when the number of hollowed-out units is varied. Therefore, two sweeping analyses are conducted at an excitation frequency of f_{exc} = 4.25, whose results are presented in Fig. 9. In Fig. 9(a), the harvester has N = 7 hollowed-out units while, in Fig. 9(b), it has N = 14. Fig. 9(a) presents the expected result, as suggested by the optimisation procedure (see Table 2). In Fig. 9(b), as expected, the overall power output is increased due to a higher number of charge transfer cycles. However, note how the optimal ratio $r_{\delta|d}$ is shifted upwards from 0.65 to 0.80 at the configuration with more hollowed-out units. Although the main conclusion remains, i.e., $r_{\delta|d}$ leads to $\delta < d$, the change in the optimal region once more indicates the complexity of the relationship between the parameters and confirms the need for an optimisation procedure to determine the optimal device configuration without the need for time-consuming sweeping analyses.

The next step in the analysis extends the optimisation to other leading parameters, such as the thickness of the dielectric layer and the number of hollowed-out units, leading to four optimisation parameters, as presented in Table 3. The results show that, overall, the power output for a sliding-mode triboelectric harvester with the same surface area as that of the prototype is more than 100 times higher by allowing the thickness of the dielectric film and the number of hollowed-out units to be optimised. The optimisation routine indicates that a higher number of hollowed-out units is more desirable. However, the gain due to the addition of hollowed-out units is beneficial up to a certain point, as already confirmed by [50,51]. Also, note that the optimal number of grating units decreases as the frequency increases, a relationship explored for the first time in the study of triboelectricity. It should be noted that all optimisation results take into account the degradation of the charge transfer efficiency caused by the decrease of the unit aspect ratio of each grating unit (δ/t_d). Thus, the model is sensitive to the negative influence of the edge effect on the power output as the number of hollowed-out units and film thickness are increased.

Table 3 shows that the harvester benefits from higher thickness when compared to the 50 μm used for the prototype. In many cases, however, the thickness of the dielectric layer assumes a value quite near the distance between two hollowed-out units ($t_d \sim \delta$), so that the unit aspect ratio for each grating unit is approximately 1. As the optimal thickness increases, the optimisation algorithm adjusted $r_{\delta|d}$ and N in order to maintain δ always greater than t_d. Thus, the optimisation routine indicates that the harvester has a better performance when $t_d \rightarrow \delta$. This is an unexpected result; when the thickness is comparable to the width of the electrodes (the distance between the hollowed units), the edge effect becomes obvious, which weakens the charge-transferring efficiency. Lower aspect ratios result in higher charge cycles. Under that condition, however, the charge transfer efficiency is around 50%. Nevertheless, the algorithm informs that having more charge cycles

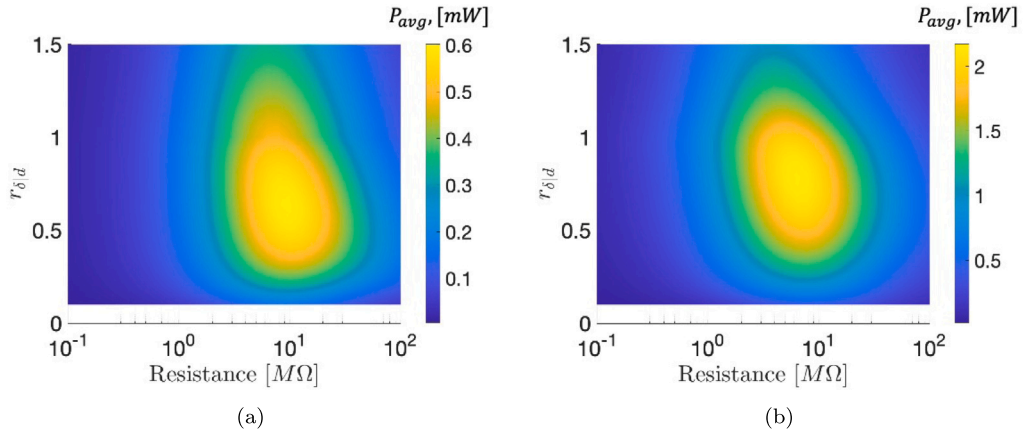

Fig. 9. Sweep analysis of the 75 mm prototype considering R and $r_{\delta|d}$: (a) with the original $N = 7$ hollowed-out units, and (b) with $N = 14$.

Table 3
Optimisation of the ratio $r_{\delta|d}$, number of hollowed-out units N, dielectric thickness t_d, and Resistance R applied to the prototype configuration obtained via surrogate optimisation under harmonic excitation.

	Device configuration									
	Optimisation parameters				Optimised parameters					
f_{exc}	$r_{\delta\|d}$	N	t_d	R	δ	d	δ/t_d	n_{dl}	P_{avg}/f	V_{RMS}
Hz	–	–	μm	MΩ	μm	μm	–	–	mW/Hz	V
0.89	0.83	184	151	28	184	222	1.22	17	19.45	169.50
1.36	0.91	137	226	29	260	286	1.15	16	16.77	203.50
1.84	0.88	100	307	33	349	397	1.14	15	14.51	243.64
2.32	0.84	116	226	20	294	350	1.30	16	12.88	194.37
2.80	0.88	76	310	29	459	522	1.48	15	12.10	255.57
3.28	0.88	82	310	23	426	484	1.37	15	10.70	234.03
3.76	0.82	84	310	22	400	488	1.29	15	9.69	230.67
4.25	0.87	71	309	20	488	561	1.58	15	9.13	230.00

(higher N value) at 50% efficiency is better than a lower number of charge cycles at higher efficiency.

Table 3 shows that, as the frequency increases, the optimal resistance tends to decrease. This tendency is observed up to the point when the film thickness suddenly increases, when R_{opt} also jumps from 16 MΩ at $f = 2.80$ Hz to 30 MΩ at 3.28 Hz. This can be explained by the fact the optimal resistance is inversely proportional to the excitation frequency and to the capacitance. Since the rise in excitation frequency is smaller than the decrease in capacitance due to the higher thickness, the optimal resistance needs to increase. Although the Equation to calculate the optimal impedance is not applicable due to the varying capacitance, the relationship it establishes is still valid.

6.2. The sliding-modetriboelectric harvester design

Fig. 10 presents the sliding-mode triboelectric harvester's design, which is comprised of a stationary and an oscillating part. The stationary component is composed of metallic layers (blue) attached to dielectric layers (yellow) while the oscillating component is composed of metallic layers (red). The metallic and dielectric layers form a grating-structured sliding-mode triboelectric generator (S-TEG). The grating pattern is identical in all layers, across electrodes and dielectric films. The harvester is excited via a host structure of length L, width W_d, and thickness T. The carriage mass, comprised of the metallic component of the triboelectric harvester, is excited under an input acceleration provided by a vibrating structure, which moves the host structure. The carriage slides along the device length, being guided by the stationary part of the device and the side rails (where the springs are located) and the carriage is connected to the host structure by spring and damper elements, similar to the design presented by [24] for a piezoelectric energy harvester.

Such a sliding-mode triboelectric harvester design is a novel approach to enable high power output. As it is composed of several triboelectric units, the device grows in complexity with new parameters being added to the performance Equation of the harvester. Consequently, new design approaches need to be considered for optimal power output. Independently designing a single triboelectric unit and arranging it as presented in Fig. 10 may not lead to its optimal performance. The device needs to be designed in the context of the application, under the operating conditions it will be submitted to. Most designs and optimisation procedures proposed with figure-of-merit methodologies limit the design to single units and within the safe condition of maintaining a high aspect ratio ($\delta/t_d > 300$). In addition to that, they do not take into consideration non-linearities from the charge transfer degradation. Therefore, in addition to presenting a full-sized triboelectric harvester solution, the harvester is submitted to a global optimisation algorithm. The global optimisation algorithm takes into consideration leading parameters that are able to affect the performance of the harvester. Therefore, each parameter is assessed considering the role it plays as the other parameters change and within applied constraints.

6.3. Optimisation of the sliding-mode triboelectric concept

As presented in Fig. 10, one triboelectric unit is comprised of two electrodes and a dielectric film placed between them. In the conductor-to-dielectric contact mode, the dielectric film is attached to the bottom electrode while the top electrode slides over the film. The tribolectric harvester is comprised of several triboelectric units, all having the same grating pattern on the electrodes and the dielectric films. However, the oscillating electrode is allowed to assume different lengths l_c according to the length ratio $r_{l|L}$ while the dielectric film and the electrode attached to it have constant lengths L_d. The sliding-mode triboelectric

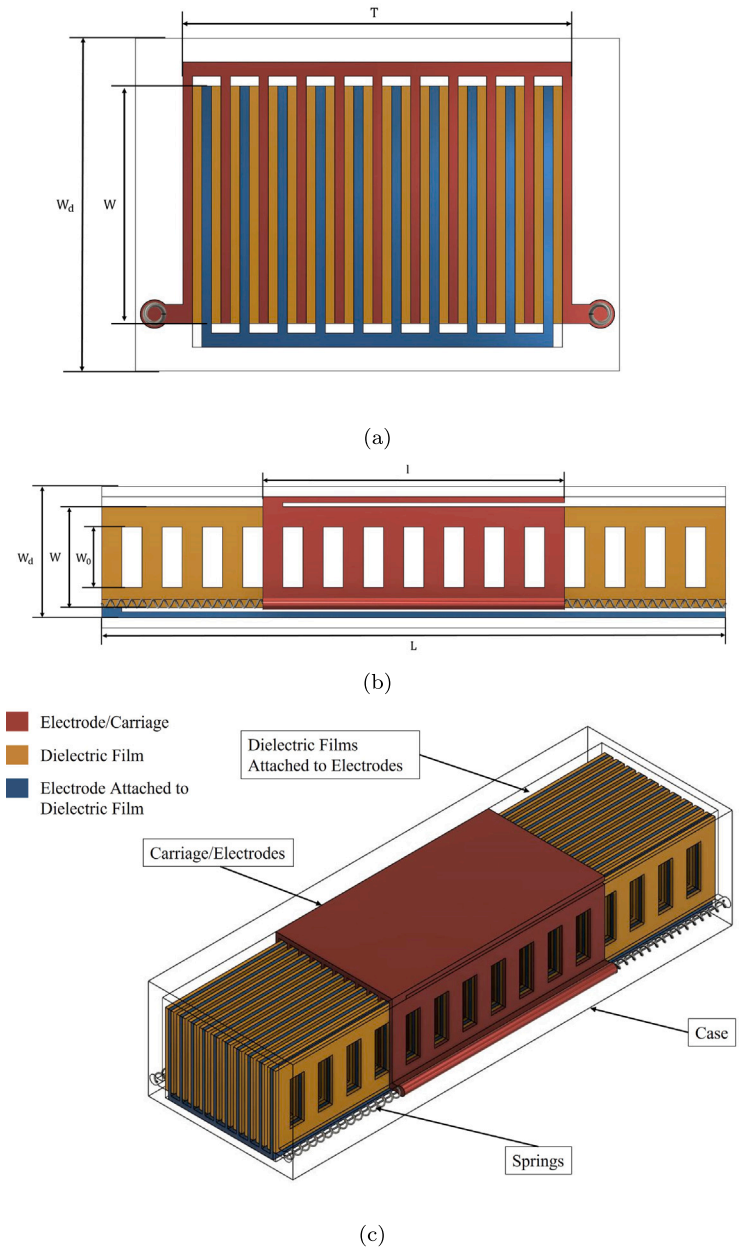

Fig. 10. Device Design: (a) Front view indicating the layers' arrangement and overall dimensions, (b) side view showing the grating pattern on film and carriage, and (c) isometric view presenting the main components of the sliding-mode triboelectric harvester.

device is analysed in five length configurations: 50, 75, 100, 150, and 200 mm, all with thickness $T_d = 20$ mm, and width $W_d = 25$ mm. Since the stationary and oscillating layers are allowed to assume distinct lengths and their grating pattern is identical, the number of hollowed-out units on them is different. Here, it is considered that the carriage/electrode can only slide along the length of the dielectric film, as illustrated in Fig. 10. Therefore, Eq. (21) establishes the following boundary condition:

$$0 \leq A \leq \frac{L_d - l_c}{2}, \tag{21}$$

where A is the amplitude of the carriage displacement $x = A\sin(\omega t)$.

There are two conditions when $L_d = l_c$ only. The first takes place when $r_{l|L} = 0$, which leads to $N = n$ according to Eq. (11) and, consequently, to $L_d = l_c$ according to Eq. (12). The second takes place when $N = 0$, which leads to $n = 0$ according to Eq. (11) and, consequently, to $L_d = l_c$ according to Eq. (12). In both cases, however, equal lengths means zero displacement amplitude, as determined by Eq. (21). Thus, the power output is also zero. This configures the main difference between the first optimisation round, which had a constant displacement amplitude applied to the system, and the one presented in this section, whose displacement amplitude depends on l_c and L_d.

Table 4 presents the optimisation results for the five length configurations of the sliding-mode triboelectric design presented in Fig. 10 under excitation frequencies ranging from 1 to 25 Hz. The first two columns present the parameters related to the motion and dimensions of the harvester, i.e., its excitation frequency f_{exc} and length L_d. These values are constant through each individual optimisation round. The width W_d and the thickness T_d of the harvester are not presented here because they remain constant across all analyses, $W_d = 25$ mm, $T_d = 20$ mm. The optimisation parameters are presented in the next five columns. These are the parameters **p** which compose the objective function. All the other variable parameters presented in the remaining columns are calculated as a result of **p**.

Table 4
Optimisation of the ratio $r_{l|L}$, $r_{\delta|d}$, number of hollowed-out units N, dielectric thickness t_d, and Resistance R applied to the sliding-mode triboelectric harvester, obtained via surrogate optimisation under harmonic excitation.

	Device configuration													
	Film	Optimisation parameters					Optimised parameters							
f_{exc}	L_d	$r_{l\|L}$	$r_{\delta\|d}$	N	t_d	R	l_c	δ	d	δ/t_d	n	n_{dl}	P_{avg}/f	V_{RMS}
Hz	mm	–	–	–	μm	MΩ	mm	μm	μm	–	–	–	mW/Hz	V
1.00	50	0.48	0.90	192	123	64	26.10	123	137	1.00	100	17	6.14	151.73
1.00	75	0.34	0.91	201	151	50	49.69	177	195	1.17	133	17	12.26	189.90
1.00	100	0.41	0.92	208	226	37	59.23	230	250	1.02	123	16	18.60	206.28
1.00	150	0.38	0.88	281	203	18	92.98	249	283	1.23	174	16	35.99	202.76
1.00	200	0.27	0.90	395	226	13	145.89	240	266	1.06	288	16	55.26	212.62
2.00	50	0.38	0.89	105	223	82	31.04	223	251	1.00	65	16	4.73	220.39
2.00	75	0.38	0.85	152	226	39	46.47	226	266	1.00	94	16	8.81	207.82
2.00	100	0.37	0.89	143	305	35	63.06	328	369	1.08	90	15	13.44	249.63
2.00	150	0.38	0.88	179	391	25	93.17	391	445	1.00	111	14	24.22	295.36
2.00	200	0.31	0.93	232	310	11	138.06	415	446	1.34	160	15	37.53	229.74
5.00	50	0.27	0.92	58	407	101	36.32	410	445	1.01	42	14	3.00	328.52
5.00	75	0.28	0.83	89	310	41	54.04	380	458	1.23	64	15	5.25	266.64
5.00	100	0.30	0.91	105	310	22	69.66	452	496	1.46	73	15	9.08	256.93
5.00	150	0.32	0.86	170	226	10	102.48	407	473	1.80	116	16	14.49	212.31
5.00	200	0.27	0.84	147	515	13	145.75	619	737	1.20	107	13	21.05	326.93
10.00	50	0.25	0.94	44	407	65	37.64	545	579	1.34	33	14	2.17	317.06
10.00	75	0.34	0.89	47	520	36	49.72	744	836	1.43	31	13	4.16	341.16
10.00	100	0.37	0.84	87	310	13	63.41	522	621	1.68	55	15	5.65	218.52
10.00	150	0.36	0.95	89	398	16	96.36	817	860	2.05	57	14	9.34	328.17
10.00	200	0.40	0.89	103	633	13	120.75	910	1023	1.44	62	12	12.59	374.01
25.00	50	0.36	0.87	36	357	24	32.17	638	733	1.79	23	14	1.46	249.50
25.00	75	0.24	0.84	40	764	39	56.46	846	1008	1.11	30	11	2.04	426.42
25.00	100	0.29	0.86	45	517	29	71.40	1017	1183	1.97	32	13	3.29	430.14
25.00	150	0.30	0.89	68	791	18	106.19	1032	1159	1.30	48	11	5.47	473.96
25.00	200	0.33	0.82	118	509	8	134.15	761	928	1.49	79	13	6.58	308.49

The outcome of the optimisation round presented in Table 4 indicates that, under the geometrical constraint applied (see Eq. (21)), the optimal length ratio $r_{l|L}$ tends to lower values, i.e., the length assumed by the carriage gives preference to higher overlap areas, rather than higher displacement amplitudes. The average power output yielded by each harvester configuration increases with the frequency and with the length, as there will be more charge transfer cycles. Note, however, that the average power per cycle decreases with the frequency so that the overall power saturates at high excitation frequencies. Fig. 11(a) shows that trend as well as the fact that, at lower frequencies, longer devices provide higher power density per cycle (P_{RMS}/L_d), indicating a non-linear relationship between the device length and the output power, Note, however, at higher frequencies, the power density per cycle is similar across all device sizes. Fig. 11(b) shows that there is a linear relationship between the log of the power density (power per area) per cubic cycle and the frequency, with a negative slope.

$$Lg\left(\frac{P_{rms}}{Af^3}\right) = b - c\ Lg(f) \tag{22}$$

where b and c are the constants defined for each device size from Fig. 11(b). This formula, based on the optimal values of the parameters, can be used to determine the power output of the device based on the dielectric area, the device size, and the operational frequency.

From Table 4 is also clear that the sliding-mode triboelectric harvester benefits from non-uniformity between the width of the hollowed-out units d and the distance between them δ, as the optimal ratio between $r_{\delta|d}$ assumes values less than one in all cases. Thus, d must always be a little greater than δ for optimal performance. In other words, the optimal unit aspect ratio tends to the unit, corroborating previous results where $\delta/t_d \sim 1$ for best performance, despite the fact that the charge transfer efficiency at that unit aspect ratio is around 50%. Another interesting trend is noticed in the overall decrease in the number of hollowed-out units with the rise in excitation frequency, which prompts the rise in the thickness of the dielectric film to maintain the unit aspect ratio near 1, as a lower number of hollowed-out units leads to greater values of d and δ.

Another critical point of analysis is explored by measuring the impact of the optimisation procedure in the design process of the sliding-mode triboelectric harvester for each excitation frequency. Therefore, the optimal parameters obtained for the 50 mm device excited at 1 and 25 Hz were selected from Table 4, and applied to all other length configurations and excitation frequencies, keeping the excitation amplitude as defined in Eq. (21). Since the resistance is commonly optimised in most energy harvesting circuits, results with optimal resistance for each configuration are also presented to allow comparing the influence of optimising the other four parameters $[t_d, r_{\delta|d}, r_{l|L}, N]$. Therefore, each chart in Fig. 12 will have three indications in their legends: Fully-Optimised (blue) for the version where all five parameters are optimised, R-Optimised (red) for the version where only the load resistance is optimised, and Not-Optimised (yellow) for the version where no parameters where optimised.

Fig. 12(a) presents the results for the 50 mm device with the optimal parameters obtained at 25 Hz. Here, the optimal parameters obtained for the 50 mm device excited at 25 Hz are applied to all other conditions and compared to the fully-optimised results (blue) as presented in Table 4. At 1 Hz, the optimised result for P_{RMS}/f is 1.96 times higher than the R-optimised result and 14.51 times higher than the non-optimised result. At 2 Hz, that difference decreases, however, the optimised result for P_{RMS}/f is still 1.62 times higher than the R-optimised result and 6.10 times higher than the non-optimised result. At 5 Hz, the optimal result is 1.23 and 2.07 times higher than the R-optimised and non-optimised results, respectively. At 10 Hz, the improvement provided by the optimisation is 1.25 and 1.38 times higher, respectively compared to the R-optimised and non-optimised results. Since the simulations are conducted using the optimisation results for the $L_d = 50$ mm at 25 Hz configuration, all three results are identical at 25 Hz. The results thus show that the improvement provided by the optimisation is clearly higher far from the intended optimisation frequency of the non-optimised cases.

The improvement provided by $[t_d, r_{\delta|d}, r_{l|L}, N]$ is more significant than the improvement provided by R only at 1 and 10 Hz. At 2 and 5 Hz, the influence of the resistance is more significant, i.e., R alone

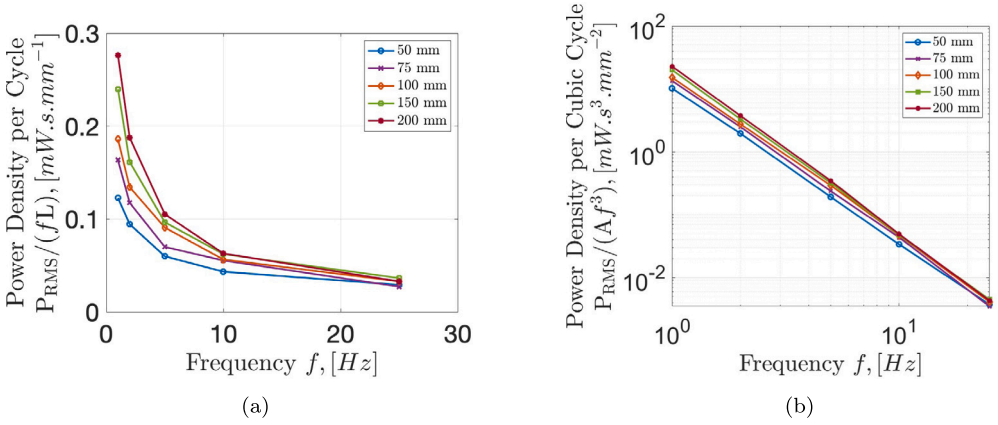

Fig. 11. Optimisation results from Table 4: (a) Power per cycle per length as the frequency increases for each length, and (b) power per cubic cycle per area as the length increases for each frequency.

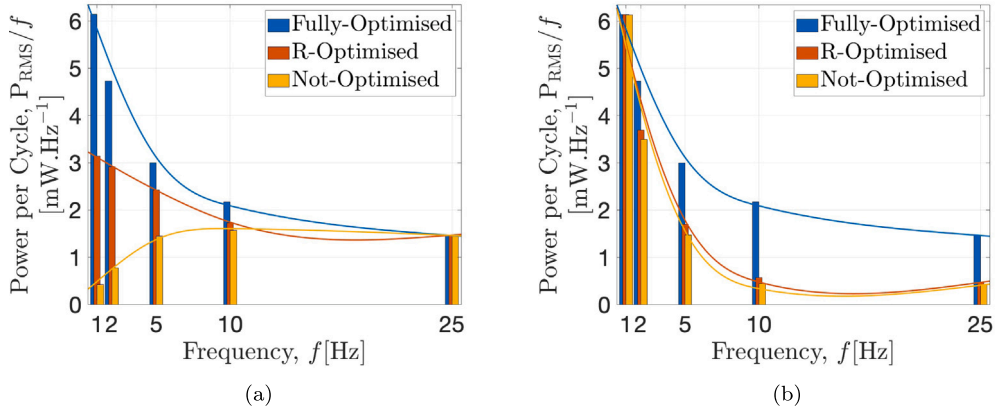

Fig. 12. Comparison between non-optimised, R-optimised, and fully-optimised sliding-mode triboelectric harvesters considering the optimal parameters from the (a) 50 mm at 25 Hz and (b) 50 mm at 1Hz configurations.

provides a greater improvement than that provided by all the other four parameters combined $[t_d, r_{\delta|d}, r_{l|L}, N]$. Observe that, at 1 Hz, the rise in P_{RMS}/f is of 2.71 mW s mm^{-1} from non-optimised to R-optimised, while of 3.00 mW s mm^{-1} from R-optimised to fully optimised. At 2 Hz, the rise in P_{RMS}/f is of 2.13 mW s mm^{-1} from non-optimised to R-optimised, while of 1.81 mW s mm^{-1} from R-optimised to fully optimised. At 5 Hz, the rise in P_{RMS}/f is of 0.98 mW s mm^{-1} from non-optimised to R-optimised, while of 0.57 mW s mm^{-1} from R-optimised to fully-optimised. At 10 Hz, the rise in P_{RMS}/f is of 0.16 mW s mm^{-1} from non-optimised to R-optimised, while of 0.44 mW s mm^{-1} from R-optimised to fully-optimised.

The same analysis is conducted considering the optimal parameters obtained for the 50 mm device excited at 1 Hz, as presented in Fig. 12(b). Similar to the pattern observed in Fig. 12(a), the optimisation is more relevant far from the optimal point, i.e., the discrepancy in P_{RMS}/f between the fully-optimised and not-optimised is more significant as the frequency increases, since the optimal parameters are meant for an excitation frequency of 1 Hz. Note, however, that the improvement provided by $[t_d, r_{\delta|d}, r_{l|L}, N]$ is more significant than the improvement provided by R in all cases.

The optimisation methodology is flexible, accepting more or fewer parameters as needed. For example, another interesting analysis can be carried out to indicate the optimal ratio between the thickness and width of the device, so that the overall cross-sectional area is kept constant. We can take this further and analyse the optimal ratio between all dimensions keeping the volume constant. Such analyses are helpful for manufacturing processes, whose machining time and cost tend to be affected by such parameters. As evidence of how those parameters can change the performance of the harvester, an additional simulation is conducted considering a device thickness of T_d = 10 mm and width of W_d = 50 mm, as opposed to the T_d = 20 mm and width of W_d = 25 mm presented in all previous analyses, keeping the overall device volume the same. The outcome of the analysis indicates that the new cross-sectional ratio is more advantageous at low frequencies, as presented in Figs. 13(a) and 13(b). However, at higher frequencies, that discrepancy tends to decrease and saturate, indicating that both configurations would present similar performances. These results give a margin for further analyses, encouraging the inclusion of other parameters that will assist in designing energy harvesters with higher performance.

Conclusions

A novel multi-unit sliding-mode triboelectric energy harvester is designed, driven by a global optimisation methodology based on the average power performance output, at varying frequencies and device's size. The original sliding-mode triboelectric governing equations are modified to offer more versatility in the analysis of the relationship between the various parameters that govern the performance of a triboelectric unit. An experimental analysis was conducted to validate the analytical model adopted, yielding satisfactory results under all excitation conditions tested. In addition to the experimental analyses, FEM simulations were conducted, also corroborating the validity of the model.

The performance optimisation of the triboelectric unit is conducted in the context of the entire harvester, taking into account the influence

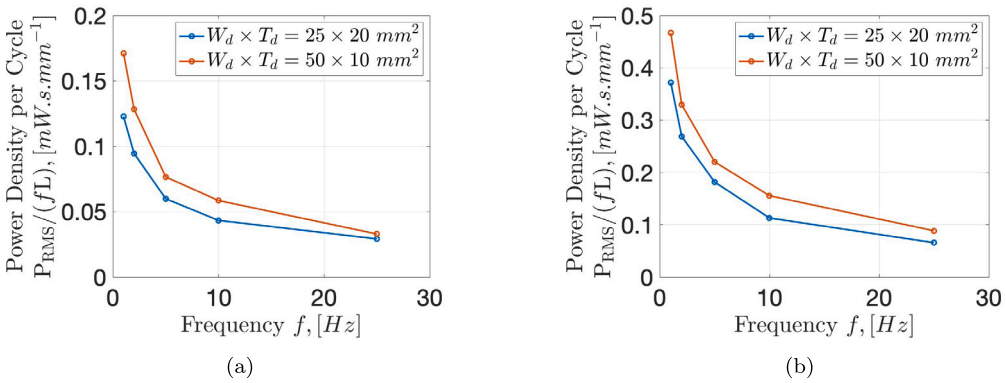

Fig. 13. Comparison between the (a) 50 mm and (b) 100 mm devices at two cross-sectional dimension ratios but same area WxT = 25 × 20 mm² (original) and 50 × 10 mm².

of the number of layers composing the device as well as the operating conditions. During the optimisation process, several parameters were varied, including the thickness of the dielectric film, the ratio between the hollowed-out units and the distance between them, the number of hollowed-out units, and the electrical resistance. Besides the consequent changes to the capacitance, open-circuit voltage, optimal resistance, and charge transfer cycles, a critical parameter changed in the process was the unit aspect ratio of the triboelectric unit. The original triboelectric models were derived based on the assumption that a high unit aspect ratio is kept. Here, a novel optimisation methodology is suggested, providing new information about the performance of triboelectric energy harvesters in conditions not previously discussed in the literature as follows:

1. A FEM analysis was incorporated to the analytical equations used in the numerical model through a charge transfer efficiency parameter, function of the unit aspect ratio, to overcome the limitation of no analytical solution to account for the charge degradation at a lower unit aspect ratio.
2. By considering the edge effect, the associated non-linearity was added to the response of the system, as observed in FEM simulations, and the code acquired more flexibility to analyse regions previously neglected due to mathematical limitations.
3. The optimal performance region was established as a trade-off between the gain from greater charge cycles and the loss from charge transfer degradation at low unit aspect ratio designs.
4. The influence of the ratio $r_{\delta|d}$ between the width of the hollowed-out units (d) and the distance between them (δ) was analysed for the first time. The results show that optimal power output is achieved when $d > \delta$, not when they are equal as adopted in grating designs in the literature [50,51]. The optimal value of this ratio may vary from 0.64 up to 0.91.
5. The influence of the ratio $r_{l|L}$ between the length of the oscillating layers and the length of the stationary layers was analysed for the first time. It has been shown that the optimal length ratio is not half as mostly adopted [50], but that it varies depending on the other parameters such as the excitation frequency and resistance.
6. The results show that the optimal number of grating units tends to decrease as the frequency increases, which shows its dependency to the excitation conditions and not only with the topology of the layers.
7. It has been shown that the optimal parameters set defined at a given operating condition is able to yield good performance under frequency range around the analysed point, demonstrating the robustness and importance of the optimisation.

The paper delivered the following new results:

1. At optimal conditions, the power per cycle tends to level off to become asymptotic, decreasing as the frequency increases for any device size.
2. The rms power density per cycle is greater for longer devices, however, the discrepancy decreases at higher frequencies.
3. Increasing the device length, i.e. contact area, is not followed by a linear increase in power density per cycle. Conversely, the power density per cycle tends to a saturation as the length of the device is increased.
4. An optimised harvester is able to generate significantly more energy when compared against their non-optimised versions. Moreover, the proposed concept's power output does not drastically drop when there are some frequency fluctuations, as was demonstrated in Fig. 12.
5. The optimisation algorithm indicates that within a given device's thickness it is better to have thicker triboelectric layers and less layers up to the region where $d \sim t_d$.
6. The turning point for the unit aspect ratio is found to be near $d \sim t_d$, where the charge degradation is around 50%. Thus, the algorithm informs that the harvester benefits more from higher charge cycles than from a 100% efficient charge transfer up to $d \sim t_d$.
7. The results obey general relationship between resistance, capacitance, and frequency showing that $R \sim 1/C\omega$. However, the algorithm also indicates the influence of $r_{d|\delta}, r_{l|L}, N$ on the optimal resistance due to their effect on the capacitance of the system.
8. The optimisation methodology is flexible, accepting more or less parameters as needed. This characteristic give margin for further analyses, encouraging the inclusion of other parameters that will assist to yield higher energy harvesting performance. Changing the cross-sectional dimension ratio from $W \times T = 25 \times 20$ mm² to $W \times T = 50 \times 10$ mm², while maintaining the area, yielded up to 31% increase in the power generated per cycle.

Optimisation procedures associated to more flexible mathematical models are shown to be of extreme importance in the design of energy harvesting systems. Here, it has been demonstrated the impact that the several parameters have on the performance of the harvester and how limitations imposed to the analytical models can prevent the analyses in parametric regions where the harvester would potentially generate more energy.

CRediT authorship contribution statement

Lucas Q. Machado: Conceptualization, Methodology, Software, Validation, Formal analysis, Investigation, Resources, Data curation, Writing – original draft, Writing – review & editing, Visualization.

Huai Zhao: Conceptualization, Resources, Writing – review & editing. **Morteza Amjadi:** Resources, Writing – review & editing, Supervision. **Huajiang Ouyang:** Resources, Writing – review & editing, Supervision. **Philippe Basset:** Conceptualization, Validation, Writing – review & editing, Supervision. **Daniil Yurchenko:** Conceptualization, Methodology, Formal analysis, Investigation, Resources, Writing – original draft, Writing – review & editing, Visualization, Supervision.

Declaration of competing interest

The authors declare that they have no known competing financial interests or personal relationships that could have appeared to influence the work reported in this paper.

Data availability

Data will be made available on request.

Acknowledgements

The authors would like to acknowledge and are thankful for the support received from the Brazilian National Council for Scientific and Technological Development—CNPq, grant 202615/2019-7. The authors would also like to acknowledge and thank the Ph.D. student Tom Jacquin for his support in providing some of the materials used in the experiments and the technician James Maxwell-Smith for his help in building the experimental rig.

References

[1] GVR, Internet of Things in retail market size report, 2021–2028, 2021, URL www.grandviewresearch.com/industry-analysis/internet-of-things-iot-retail-market.

[2] S. Kumar, P. Tiwari, M. Zymbler, Internet of Things is a revolutionary approach for future technology enhancement: a review, J. Big Data 6 (1) (2019) 111, http://dx.doi.org/10.1186/s40537-019-0268-2.

[3] Z.J. Chew, Y. Kuang, T. Ruan, M. Zhu, Energy harvesting in smart cities, in: Handbook of Smart Cities, Springer International Publishing, Cham, 2021, pp. 593–620, http://dx.doi.org/10.1007/978-3-030-69698-6_35.

[4] B. Munir, V. Dyo, On the impact of mobility on battery-less RF energy harvesting system performance, Sensors 18 (11) (2018) http://dx.doi.org/10.3390/s18113597.

[5] Y. Xie, S. Wang, S. Niu, L. Lin, Q. Jing, J. Yang, Z. Wu, Z.L. Wang, Grating-structured freestanding triboelectric-layer nanogenerator for harvesting mechanical energy at 85% total conversion efficiency, Adv. Mater. 26 (38) (2014) 6599–6607, http://dx.doi.org/10.1002/adma.201402428.

[6] L. Lin, S. Wang, Y. Xie, Q. Jing, S. Niu, Y. Hu, Z.L. Wang, Segmentally structured disk triboelectric nanogenerator for harvesting rotational mechanical energy, Nano Lett. 13 (6) (2013) 2916–2923, http://dx.doi.org/10.1021/nl4013002, PMID: 23656350.

[7] R. Wang, J. Cui, Y. Liu, D. Liu, C. Du, S. Yan, Y. Zheng, C. Xue, Multi-pulse triboelectric nanogenerator based on micro-gap corona discharge for enhancement of output performance, Energy 244 (2022) 122588.

[8] S. Niu, Y. Liu, S. Wang, L. Lin, Y.S. Zhou, Y. Hu, Z.L. Wang, Theory of sliding-mode triboelectric nanogenerators, Adv. Mater. 25 (43) (2013) 6184–6193, http://dx.doi.org/10.1002/adma.201302808.

[9] Z.L. Wang, L. Lin, J. Chen, S. Niu, Y. Zi, Harvesting body motion energy, in: Triboelectric Nanogenerators, Springer International Publishing, Cham, 2016, pp. 207–236, http://dx.doi.org/10.1007/978-3-319-40039-6_8.

[10] X. Chen, J. He, L. Song, Z. Zhang, Z. Tian, T. Wen, C. Zhai, Y. Chen, J. Cho, X. Chou, C. Xue, Flexible one-structure arched triboelectric nanogenerator based on common electrode for high efficiency energy harvesting and self-powered motion sensing, AIP Adv. 8 (4) (2018) 045022, http://dx.doi.org/10.1063/1.5027659.

[11] L. Gao, S. Lu, W. Xie, X. Chen, L. Wu, T. Wang, A. Wang, C. Yue, D. Tong, W. Lei, H. Yu, X. He, X. Mu, Z.L. Wang, Y. Yang, A self-powered and self-functional tracking system based on triboelectric-electromagnetic hybridized blue energy harvesting module, Nano Energy 72 (2020) 104684, http://dx.doi.org/10.1016/j.nanoen.2020.104684.

[12] G. Cheng, H. Zheng, F. Yang, L. Zhao, M. Zheng, J. Yang, H. Qin, Z. Du, Z.L. Wang, Managing and maximizing the output power of a triboelectric nanogenerator by controlled tip–electrode air-discharging and application for UV sensing, Nano Energy 44 (2018) 208–216, http://dx.doi.org/10.1016/j.nanoen.2017.11.062.

[13] D. Macário, I. Domingos, N. Carvalho, P. Pinho, H. Alves, Harvesting circuits for triboelectric nanogenerators for wearable applications, iScience 25 (4) (2022) 103977, http://dx.doi.org/10.1016/j.isci.2022.103977.

[14] Y. Zou, V. Raveendran, J. Chen, Wearable triboelectric nanogenerators for biomechanical energy harvesting, Nano Energy 77 (2020) 105303, http://dx.doi.org/10.1016/j.nanoen.2020.105303.

[15] I. Kim, D. Kim, 3D printed double roller-based triboelectric nanogenerator for blue energy harvesting, Micromachines 12 (9) (2021) http://dx.doi.org/10.3390/mi12091089.

[16] H. Chen, C. Xing, Y. Li, J. Wang, Y. Xu, Triboelectric nanogenerators for a macro-scale blue energy harvesting and self-powered marine environmental monitoring system, Sustain. Energy Fuels 4 (2020) 1063–1077, http://dx.doi.org/10.1039/C9SE01184F.

[17] C. Zhang, L. He, L. Zhou, O. Yang, W. Yuan, X. Wei, Y. Liu, L. Lu, J. Wang, Z.L. Wang, Active resonance triboelectric nanogenerator for harvesting omnidirectional water-wave energy, Joule 5 (6) (2021) 1613–1623, http://dx.doi.org/10.1016/j.joule.2021.04.016.

[18] P. Kanokpaka, L.-Y. Chang, B.-C. Wang, T.-H. Huang, M.-J. Shih, W.-S. Hung, J.-Y. Lai, K.-C. Ho, M.-H. Yeh, Self-powered molecular imprinted polymers-based triboelectric sensor for noninvasive monitoring lactate levels in human sweat, Nano Energy 100 (2022) 107464, http://dx.doi.org/10.1016/j.nanoen.2022.107464.

[19] J. Chen, C. Zhang, W. Xuan, L. Yu, S. Dong, Y. Xie, W. Yin, J. Luo, Triboelectric nanogenerator-based self-powered resonant sensor for non-destructive defect detection, Sensors (Basel) 19 (15) (2019).

[20] M. Alzgool, Y. Tian, B. Davaji, S. Towfighian, Self-powered triboelectric MEMS accelerometer, Nano Energy 109 (2023) 108282, http://dx.doi.org/10.1016/j.nanoen.2023.108282.

[21] H.M.A. Hamid, Z. Çelik-Butler, A novel MEMS triboelectric energy harvester and sensor with a high vibrational operating frequency and wide bandwidth fabricated using UV-LIGA technique, Sensors Actuators A 313 (2020) 112175, http://dx.doi.org/10.1016/j.sna.2020.112175.

[22] M. Alzgool, M. Mousavi, B. Davaji, S. Towfighian, Micro-triboelectric generator for zero-power shock detection, Nano Energy 103 (2022) 107758, http://dx.doi.org/10.1016/j.nanoen.2022.107758.

[23] L.Q. Machado, D. Yurchenko, J. Wang, G. Clementi, S. Margueron, A. Bartasyte, Multi-dimensional constrained energy optimization of a piezoelectric harvester for E-gadgets, iScience 24 (7) (2021).

[24] L.Q. Machado, P. Alevras, D. Tcherniak, J. Wang, S. Zhou, D. Yurchenko, Optimisation of a forced multi-beam piezoelectric energy harvester, Energy Convers. Manage. 270 (2022) 116257, http://dx.doi.org/10.1016/j.enconman.2022.116257.

[25] D. Yurchenko, L.Q. Machado, J. Wang, C. Bowen, S. Sharkh, M. Moshrefi-Torbati, D.V. Val, Global optimisation approach for designing high-efficiency piezoelectric beam-based energy harvesting devices, Nano Energy 93 (2022) 106684.

[26] R. Hinchet, A. Ghaffarinejad, Y. Lu, J.Y. Hasani, S.-W. Kim, P. Basset, Understanding and modeling of triboelectric-electret nanogenerator, Nano Energy 47 (2018) 401–409, http://dx.doi.org/10.1016/j.nanoen.2018.02.030.

[27] Y. Pang, Y. Cao, M. Derakhshani, Y. Fang, Z.L. Wang, C. Cao, Hybrid energy-harvesting systems based on triboelectric nanogenerators, Matter 4 (1) (2021) 116–143, http://dx.doi.org/10.1016/j.matt.2020.10.018.

[28] Y.S. Choi, S.-W. Kim, S. Kar-Narayan, Materials-related strategies for highly efficient triboelectric energy generators, Adv. Energy Mater. 11 (7) (2021) 2003802, http://dx.doi.org/10.1002/aenm.202003802.

[29] S. Paria, S.K. Si, S.K. Karan, A.K. Das, A. Maitra, R. Bera, L. Halder, A. Bera, A. De, B.B. Khatua, A strategy to develop highly efficient TENGs through the dielectric constant, internal resistance optimization, and surface modification, J. Mater. Chem. A 7 (2019) 3979–3991, http://dx.doi.org/10.1039/C8TA11229K.

[30] L. Lapčinskis, A. Linarts, K. Mālnieks, H. Kim, K. Rubenis, K. Pudzs, K. Smits, A. Kovaļovs, K. Kalniņš, A. Tamm, C.K. Jeong, A. Šutka, Triboelectrification of nanocomposites using identical polymer matrixes with different concentrations of nanoparticle fillers, J. Mater. Chem. A 9 (2021) 8984–8990, http://dx.doi.org/10.1039/D0TA12441A.

[31] S.S. Won, M. Kawahara, C.W. Ahn, J. Lee, J. Lee, C.K. Jeong, A.I. Kingon, S.-H. Kim, Lead-free Bi0.5(Na0.78K0.22)TiO3 nanoparticle filler–elastomeric composite films for paper-based flexible power generators, Adv. Electron. Mater. 6 (2) (2020) 1900950, http://dx.doi.org/10.1002/aelm.201900950.

[32] A. Ghaffarinejad, J.Y. Hasani, R. Hinchet, Y. Lu, H. Zhang, A. Karami, D. Galayko, S.-W. Kim, P. Basset, A conditioning circuit with exponential enhancement of output energy for triboelectric nanogenerator, Nano Energy 51 (2018) 173–184, http://dx.doi.org/10.1016/j.nanoen.2018.06.034.

[33] X. Xia, H. Wang, P. Basset, Y. Zhu, Y. Zi, Inductor-free output multiplier for power promotion and management of triboelectric nanogenerators toward self-powered systems, ACS Appl. Mater. Interfaces 12 (5) (2020) 5892–5900, http://dx.doi.org/10.1021/acsami.9b20060, PMID: 31913007.

[34] Z. Saadatnia, E. Esmailzadeh, H.E. Naguib, High performance triboelectric nanogenerator by hot embossing on self-assembled micro-particles, Adv. Eng. Mater. 21 (1) (2019) 1700957, http://dx.doi.org/10.1002/adem.201700957.

[35] Y. Shao, C. ping Feng, B. wen Deng, B. Yin, M. bo Yang, Facile method to enhance output performance of bacterial cellulose nanofiber based triboelectric nanogenerator by controlling micro-nano structure and dielectric constant, Nano Energy 62 (2019) 620–627, http://dx.doi.org/10.1016/j.nanoen.2019.05.078.
[36] K.C. Pradel, N. Fukata, Systematic optimization of triboelectric nanogenerator performance through surface micropatterning, Nano Energy 83 (2021) 105856, http://dx.doi.org/10.1016/j.nanoen.2021.105856.
[37] J.-H. Zhang, Y. Zhang, N. Sun, Y. Li, J. Du, L. Zhu, X. Hao, Enhancing output performance of triboelectric nanogenerator via large polarization difference effect, Nano Energy 84 (2021) 105892, http://dx.doi.org/10.1016/j.nanoen.2021.105892.
[38] Y. Lyu, Y. Wang, Output optimization of biodegradable triboelectric nanogenerators, Nano Energy 103 (2022) 107811, http://dx.doi.org/10.1016/j.nanoen.2022.107811.
[39] S. Cui, L. Zhou, D. Liu, S. Li, L. Liu, S. Chen, Z. Zhao, W. Yuan, Z.L. Wang, J. Wang, Improving performance of triboelectric nanogenerators by dielectric enhancement effect, Matter 5 (1) (2022) 180–193, http://dx.doi.org/10.1016/j.matt.2021.10.019.
[40] S. Niu, Z.L. Wang, Theoretical systems of triboelectric nanogenerators, Nano Energy 14 (2015) 161–192, http://dx.doi.org/10.1016/j.nanoen.2014.11.034, Special issue on the 2nd International Conference on Nanogenerators and Piezotronics (NGPT 2014).
[41] J. Shao, D. Liu, M. Willatzen, Z.L. Wang, Three-dimensional modeling of alternating current triboelectric nanogenerator in the linear sliding mode, Appl. Phys. Rev. 7 (1) (2020) http://dx.doi.org/10.1063/1.5133023.
[42] Z.L. Wang, On Maxwell's displacement current for energy and sensors: the origin of nanogenerators, Mater. Today 20 (2) (2017) 74–82, http://dx.doi.org/10.1016/j.mattod.2016.12.001.
[43] Z.L. Wang, Triboelectric nanogenerator (TENG)—Sparking an energy and sensor revolution, Adv. Energy Mater. 10 (17) (2020) 2000137, http://dx.doi.org/10.1002/aenm.202000137.
[44] K. Dai, X. Wang, S. Niu, F. Yi, Y. Yin, L. Chen, Y. Zhang, Z. You, Simulation and structure optimization of triboelectric nanogenerators considering the effects of parasitic capacitance, Nano Res. 10 (1) (2017) 157–171, http://dx.doi.org/10.1007/s12274-016-1275-7.
[45] J. Shao, M. Willatzen, Y. Shi, Z.L. Wang, 3D mathematical model of contact-separation and single-electrode mode triboelectric nanogenerators, Nano Energy 60 (2019) 630–640, http://dx.doi.org/10.1016/j.nanoen.2019.03.072.
[46] S. Niu, Y.S. Zhou, S. Wang, Y. Liu, L. Lin, Y. Bando, Z.L. Wang, Simulation method for optimizing the performance of an integrated triboelectric nanogenerator energy harvesting system, Nano Energy 8 (2014) 150–156, http://dx.doi.org/10.1016/j.nanoen.2014.05.018.
[47] H. Zhang, L. Yao, L. Quan, X. Zheng, Theories for triboelectric nanogenerators: A comprehensive review, Nanotechnol. Rev. 9 (1) (2020) 610–625, http://dx.doi.org/10.1515/ntrev-2020-0049.
[48] S. Niu, Y. Liu, S. Wang, L. Lin, Y.S. Zhou, Y. Hu, Z.L. Wang, Theory of sliding-mode triboelectric nanogenerators, Adv. Mater. 25 (43) (2013) 6184–6193.
[49] H. Zou, Y. Zhang, L. Guo, P. Wang, X. He, G. Dai, H. Zheng, C. Chen, A.C. Wang, C. Xu, Z.L. Wang, Quantifying the triboelectric series, Nature Commun. 10 (1) (2019) 1427, http://dx.doi.org/10.1038/s41467-019-09461-x.
[50] S. Niu, S. Wang, Y. Liu, Y.S. Zhou, L. Lin, Y. Hu, K.C. Pradel, Z.L. Wang, A theoretical study of grating structured triboelectric nanogenerators, Energy Environ. Sci. 7 (2014) 2339–2349, http://dx.doi.org/10.1039/C4EE00498A.
[51] H. Zhao, H. Ouyang, A vibro-impact triboelectric energy harvester with a magnetic bistable mechanism and grating-patterned films for dual power enhancement, Mech. Syst. Signal Process. 178 (2022) 109318, http://dx.doi.org/10.1016/j.ymssp.2022.109318.

Lucas Q. Machado

Huai Zhao

Morteza Amjadi

Huajiang Ouyang

Philippe Basset

Daniil Yurchenko